Diogo Miguel Mendes Ferreira Vitorino

Licenciado em Ciências de Engenharia Mecânica

Tungsten Inert Gas Welding of Ni-rich NiTiHf High Temperature Shape Memory Alloy

Dissertação para a obtenção do Grau de Mestre em Engenharia Mecânica

Orientador: Professor Doutor João Pedro de Sousa Oliveira, Faculdade de Ciências e Tecnologias da Universidade Nova de Lisboa

September 2019

Tungsten Inert Gas Welding of Ni-rich NiTiHf High Temperature Shape Memory Alloy

Ao nosso avô Zé.

Sei que estarias orgulhoso!

Acknowledgements

First and foremost, I would like express my regards to everyone who helped me during the past few months, which were entirely dedicated to the present work, mainly my adviser, Professor João Pedro Oliveira, for all the support. Additionally, all the people currently working at the Industrial Technologies centre of DEMI, FCT, including the PhD and Master's students and, particularly, Mr. Paulo Magalhães and Mr. António Campos, whose help was crucial.

My best regards go to Professor Francisco Braz Fernandes and Eng. Edgar Camancho at CENIMAT, both for allowing access to important equipment and for the support in handling it.

I am grateful to Dr. Othmane Benafan and everyone at the NASA Glenn Research Center for conducting the mechanical tests at high temperature, thus providing critical data to attain solid and useful conclusions.

I believe it is important to show my appreciation to everyone around the world who invest so much time in developing free access software, such as Octave and Fiji (ImageJ), which were used in this work. In a world where digital tools are of the greatest importance, science can only advance if these open-access tools exist.

Finally and equally importantly, to my family and friends: Thank you!

Abstract

High temperature shape memory alloys (HTSMAs) have great potential for applications in aerospace engineering mainly due to superelasticity (SE) and shape memory effect (SME) above 100 °C. Nevertheless, these alloys are seldom used in the industry, partly due to the difficult production of complex geometries, frequently needed in engineering.

Among the most studied HTSMAs, the nickel-titanium-hafnium (NiTiHf) alloy is often considered the best. Following the need for readily available complex geometries, welding this alloy through a common process, such as tungsten inert gas (TIG) welding, would make such geometries available for practical use.

The objective of this work was to weld, using tungsten inert gas technology, a Ni-rich NiTiHf alloy ($Ni_{50.3}Ti_{29.7}Hf_{20}$ (at.%)), in the form of 5 mm diameter rods, for which an automated prototype was designed, adapting manual welding equipment. The resulting welds were studied and characterised through optical microscopy, scanning electron microscopy, the Vickers hardness test, differential scanning calorimetry and mechanical testing.

Sound weld beads were accomplished, with full penetration. After heat-treatment (550 °C for 3 h), SME and SE above 100 °C were observed. Mechanical tests revealed that the welded rods have potential to be employed as solid-state actuators.

Keywords: high temperature shape memory alloy, NiTiHf alloy, TIG welding, shape memory effect, superelasticity.

Resumo

As ligas de memória de forma de alta temperatura (HTSMA) apresentam grande potencial para aplicações em engenharia, sobretudo aerospacial, devido ao efeito de memória de forma e à superelasticidade acima de 100 °C. No entanto, a sua rara utilização deve-se, em parte, à dificuldade em produzir geometrias complexas, frequentemente utilizadas em engenharia.

Entre as ligas HTSMA, a liga de níquel-titânio-háfnio (NiTiHf) é frequentemente considerada a melhor. Devido à dificuldade em obter geometrias complexas, a possibilidade de soldar esta liga através de tecnologia comum poderá facilitar a sua utilização em aplicações práticas.

O objetivo deste estudo foi soldar a liga NiTiHf ($Ni_{50.3}Ti_{29.7}Hf_{20}$ (at.%)), rica em níquel, utilizando tecnologia TIG (*tungsten inert gas*), na forma de varões com 5 mm de diâmetro. Para este efeito, um protótipo foi projetado e construído, adaptando equipamento de soldadura TIG manual. As soldaduras resultantes foram estudadas através de microscopia ótica, microscopia eletrónica de varrimento, testes de dureza Vickers, varredura diferencial de calorimetria e testes mecânicos.

Cordões sãos foram conseguidos, com penetração total. Após tratamento térmico (550 °C durante 3 h), o efeito de memória de forma e a superelasticidade acima de 100 °C foram verificados. Os testes mecânicos revelaram que os varões soldados podem ser utilizados como atuadores *solid-state*.

Palavras-chave: liga de memória de forma de alta temperatura, liga NiTiHf, soldadura TIG, efeito de memória de forma, superelasticidade.

Contents

List of Tables

List of Figures

Nomenclature

Abbreviations

A_f	Austenite finish temperature
A_p	Austenite peak
A_s	Austenite start temperature
AC	Alternated current
Au	Gold (chemical element)
AW	As-welded
BM	Base material
DC	Direct current
DCEN	Direct current electrode negative
DCEP	Direct current electrode positive
DSC	Differential scanning calorimetry
e.g.	For example
FZ	Fusion zone
HAZ	Heat affected zone
Hf	Hafnium (chemical element)
HT	Heat-treated
i.e.	That is
M_f	Martensite finish temperature
M_p	Martensite peak
M_s	Martensite start temperature
MEMS	Microelectromechanical systems
MIG/MAG	Metal inert gas / metal active gas

Ni	Nickel (chemical element)
NiTi	Nickel-titanium alloy
NiTiHf	Nickel-titanium-hafnium alloy
PC	Personal computer
Pd	Palladium (chemical element)
Pt	Platinum (chemical element)
RPM	Rotations per minute
SE	Superelasticity
SEM	Scanning electron microscopy
SIM	Stress induced martensite
SMA	Shape memory alloy
SME	Shape memory effect
TEM	Transmission electron microscopy
Ti	Titanium (chemical element)
TIG	Tungsten inert gas welding
TTs	Transformation temperatures
TWSME	Two way shape memory effect
UK	United Kingdom
USA	United States of America
Zr	Zirconium (chemical element)

Symbols

ϵ_{rec}	Recoverable strain
ϵ_{irr}	Irrecoverable strain
σ	Stress
σ_{DT}	Detwinning/reorientation stress
σ_y	Yield strength
σ_{SIM}	Stress induced martensite stress

1

Introduction

Shape memory alloys (SMAs) are a class of materials that present both superelasticity (SE) and shape memory effect (SME). Consequently, when deformed, they are able to recover their original shape upon unloading or heating, respectively. The mechanism behind these effects, called the *reversible martensitic transformation*, relies on a reversible phase transformation between austenite and martensite. The existence of any of these phases is determined by temperature and/or applied stress. SMAs that undergo the reversible martensitic transformation above 100 °C are considered high temperature shape memory alloys (HTSMAs).

SME and SE, coupled with other SMAs-typical characteristics, make HTSMAs highly interesting and potentially applicable in several industries, mainly aerospace. For instance, complex systems such as hydraulic assemblies can be replaced by simpler HTSMA actuators that take advantage of the shape memory effect, thus reducing volume and the amount of maintenance needed. Furthermore, HTSMA have been employed in aircraft engines (gas turbines) to select between high power delivery or high efficiency, in real time.

Due to few but critical disadvantages of HTSMAs, particularly the ability to manufacture components with the pretended properties, their development has been slow, as has their increasing use in the industry. The production of complex geometries, commonly needed in engineering, is particularly challenging and one way to facilitate it would be to weld simpler parts into one.

Among the several existing high temperature shape memory alloys, the nickel-titanium-hafnium (NiTiHf) alloy is often considered the best due to its mechanical and thermal properties and lower cost when compared to other NiTi-based alloys. The properties of this alloy are greatly influenced by the presence of the *H-phase*, a precipitate created during heat treatment. This precipitate is responsible for the good mechanical and thermal properties of the alloy, as was confirmed in this work.

Following the promising results obtained by other authors in laser welding of NiTiHf [2], it is reasonable to believe that tungsten inert gas (TIG) welding of the alloy can result in high quality welds. Being a versatile and common welding technology in the industry, the possibility to use this welding process to join NiTiHf parts would facilitate the alloy's use in engineering applications.

The objective of the present work is to study the feasibility of obtaining defect-free weld beads in 5 mm diameter NiTiHf alloy rods using common TIG welding equipment.

In Chapter 2, literature review is presented, where some concepts are introduced, important for the understanding of the qualities and difficulties associated with the NiTiHf alloy, namely the reversible martensitic effect, which is responsible for the most significant shape memory alloy's properties: superelasticity and shape memory effect. Additionally, TIG welding fundamentals are reviewed, namely energy source, types of current and im-

portance of the shielding gas. This subject was not deeply investigated as it is a consolidated process, hence it is not considered "state of the art".

Chapter 3 exposes the experimental procedure that was followed and discusses what was necessary to accomplished the objectives set. The following chapter, Chapter 4, discusses the tests conducted to characterise the weld beads, namely optical microscopy, *scanning electron microscopy* (SEM), *Vickers* hardness test, *differential scanning calorimetry* (DSC) and thermal cycling at constant stress.

Finally, Chapter 5 briefly presents the conclusions taken form this work and leaves some suggestions for future research.

2

Literature review

2.1 SME and SE

A material that presents *shape memory effect* (SME) has the ability to "remember" its original shape after being deformed, while *superelasticity* (SE) allows strain to reach higher values than what would be expected from most metallic materials. Both these effects (schematically represented in Figure 2.1) are highly interesting both from an academic point of view and for practical applications. Some industries may considerably benefit from such properties, namely the aerospace, automotive, mechanical, oil and gas, biomedical and potentially civil ones [3–7].

Both SME and SE rely on what is called the *reversible martensitic transformation* [5, 7, 9]. This is the result of a short coordinated shear movement of atoms, which keep close relations to each other, hence being considered a diffusionless solid state transformation [5, 7, 10].

The reversible transformation occurs between two phases and depends on temperature, applied stress or magnetic field (in the case of ferromagnetic alloys) [3, 5, 7]. Such phases may either be austenite, (cubic B2 [1], commonly

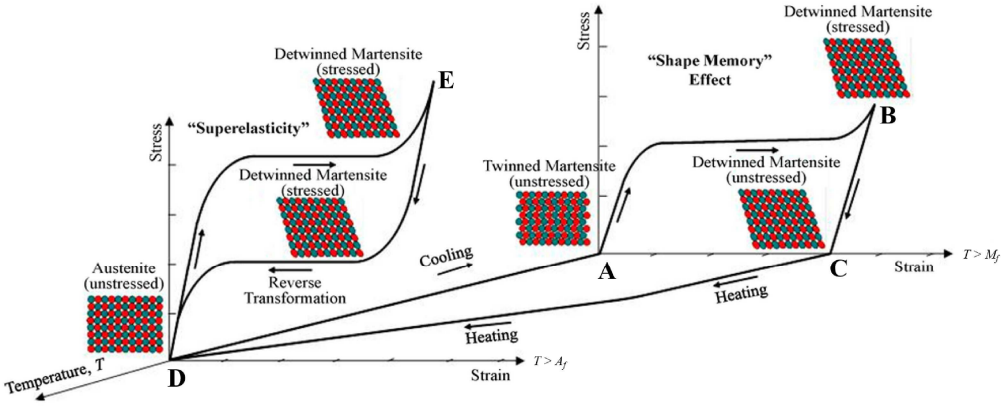

Figure 2.1: Superelasticity and shape memory effects [8]

referred to as *parent phase*), or martensite (monoclinic B19' [1]). In a neutral stress state, the former exists at high temperatures, while the latter is a low temperature phase. It is important to note that the "high" or "low" concepts are relative to a set of temperature values called *transformation temperatures* (TTs), which will be discussed later. Transformation from austenite to martensite is considered to be the forward (or direct) transformation [2,7,11], thus the reverse happens when austenite grows in martensite.

Should austenite be cooled below a certain temperature value (named M_f), the structure becomes fully martensitic (i.e. direct transformation occurs), although the macroscopic shape is not altered significantly. Hereupon, if stress is applied to martensite, deformation takes place, as shown in Figure 2.1 (A - B), and it is kept upon unloading (C), as expected. When the material is heated up again (C - D), austenite grows in martensite, forcing the macroscopic, undeformed shape to be recovered. This is known as *shape memory effect* (SME) [5,7].

Upon forward transformation, martensite may be formed in one of many

[1] relative to Nickel-Titanium and Nickel-Titanium-Hafnium alloys' crystal structure

possible orientations relative to the austenite structure. These orientations, called *martensite lattice correspondence variants*, are the result of local strain created by the difference in the austenite and martensite crystal structures [5]. In order to mitigate such strain, martensite forms *twinned* related lattice correspondence variants, which result in what is called a *habit plane variant*. No one lattice orientation or habit plane variant is energetically favoured relative to any other, unless an external load is applied, in which case the energetically favoured habit plane variants will grow at the expense of others, resulting in martensite reorientation [5]. Similarly, favoured lattice correspondence variants may grow, undertaking others, in what is called martensite *detwinning*. This results in a negligible macroscopic change [7]. Upon unloading, no change occurs since all lattice correspondence variants and habit plane variants are energetically equivalent to each other. Nonetheless, should the reverse transformation happen, austenite's crystal structure is recovered, restoring the original macroscopic shape [5].

Martensitic transformation also gives rise to the superelasticity effect, that happens when stress is applied to the material (D - E in Figure 2.1) at high temperature (i.e. austenitic phase). Due to such stress, some directions become energetically favoured, leading to an ordered growth of martensite in the austenitic phase so that deformation is accommodated. Hence, it is unlikely that twinned habit planes are formed. Once stress is released, the original shape is recovered (E - D) [7], since austenite is the phase that occurs naturally at these high temperatures and its macroscopic shape is fixed. Stress induced martensitic transformation (superelasticity) may lead to strains up to 20 % [5].

It is clear that temperature values are of great importance for SME and SE and it is important to note that transformations, either forward or reverse,

do not happen at a single temperature value but rather within a range of temperatures. Forward transformation (austenite to martensite) begins at a temperature value called M_s and ends at M_f, so below this interval only martensite exists. Since this transformation occurs upon cooling, $M_s > M_f$. Similarly, while heating, the reverse transformation begins at A_s and ceases at A_f ($A_s < A_f$) [12]. This set of temperature values (A_s, A_f, M_s and M_f) is usually referred to as transformation temperatures (TTs) [5, 7]. Another value worth pointing out is M_d, above which dislocation slip occurs before stress induced martensite as the material is gradually loaded, resulting in a normal plastic behaviour in opposition to superelasticity [5, 7].

As TTs depend on applied stress, the relationship between these two variables can be described by the Clausius-Clapeyron relationship, which roughly states that $d\sigma/dT$ is a constant [5, 12], as represented by the sloped straight lines in Figure 2.2. Although being an oversimplification of reality as it is derived only from thermodynamic relationships, ignoring certain aspects such as the effect of microstructural features, this relationship provides a general idea of the behaviour of TTs for different stress states [5].

Each SME or SE cycle is associated with an hysteresis, either thermal or stress. In practice, strain is usually not fully recovered as a consequence of plastic deformation, which may occur to some degree, due to stabilised martensite in which austenite may not form unless the alloy is heated up to higher temperatures [5]. Hence, there is a recoverable strain (ϵ_{rec} shown in Figure 2.1 as the difference in strain from A to B) and an irrecoverable strain (ϵ_{irr}) [5]. These two factors are particularly important when the objective is to employ SME as the moving force of an actuator, where work output is key. Furthermore, ϵ_{rec} is comprised of an elastic strain (difference in strain form B to C in Figure 2.1) and a shape strain (strain difference from A to C) [5].

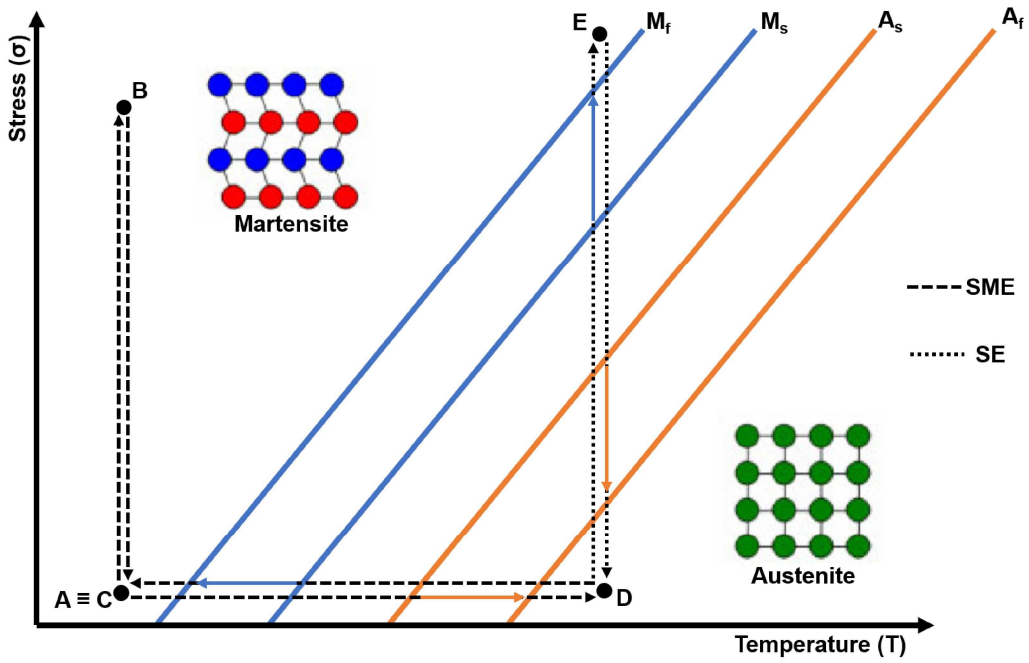

Figure 2.2: Simplified behaviour of TTs (adapted from [5])

The latter is due to the martensitic transformation, meaning it is recovered upon new transformation. Figure 2.1 does not present irrecoverable strain as it shows an ideal cycle.

Yield strength, σ_y (of which there are usually two values, one for austenite and one for martensite), is also an important factor, particularly when compared to the stress level at which martensite is stress induced in austenite, σ_{SIM}, and the stress at which martensite becomes detwinned (and/or reoriented), σ_{DT}. Should σ_y be lower than σ_{SIM}, the austenitic material becomes plastically deformed upon loading, instead of having superelasticity occur. Similarly, for σ_y values lower than σ_{DT}, plastic deformation occurs in martensite, eliminating the possibility of the shape memory effect.

These three values (σ_y, σ_{SIM} and σ_{DT}) change accordingly to temperature (Figure 2.3), where σ_y tends to decrease as temperature rises, both in

austenite and martensite. It should be noted that these values are nominal, i.e. transformation does not occur at a single stress value, but rather within a range of values [7]. Nevertheless, it is pretended that such range is as short as possible and it is reasonable to consider only the nominal values. While σ_{DT} tends to behave similarly to σ_y, σ_{SIM} usually increases with increasing temperature values [5]. It is crucial to attend to these behaviours since plastic deformation should not occur before detwinning/reorientation in martensite or before stress induced martensite (SIM) replaces austenite, at the risk of losing SME or SE, which may happen for temperatures higher than one given value, M_d. Local plastic deformation may occur for lower stress levels than σ_y, as local stress values may be higher than those resulting form externally applied loads [5], thus σ_y values are wanted as high as high as possible compared to σ_{DT} and particularly σ_{SIM}.

Another shape memory behaviour worth discussing is the two-way shape memory effect (TWSME), which is only possible when martensite is able to recall its undeformed shape, like austenite does [7]. This happens under special circumstances, when some variants are energetically favoured toward others, most likely as the result of plastic deformation in martensite or ageing under stress [5]. Although very interesting from an academic perspective and potentially highly applicable in engineering, TWSME is difficult to obtain and its recoverable strain is usually very small [5].

2.2 Shape memory alloys

The martensitic phase transformation is only possible in materials known as shape memory alloys (SMAs) [10], which are a class of smart [3] or functional [2,7] materials. As they undergo the martensitic transformation, these

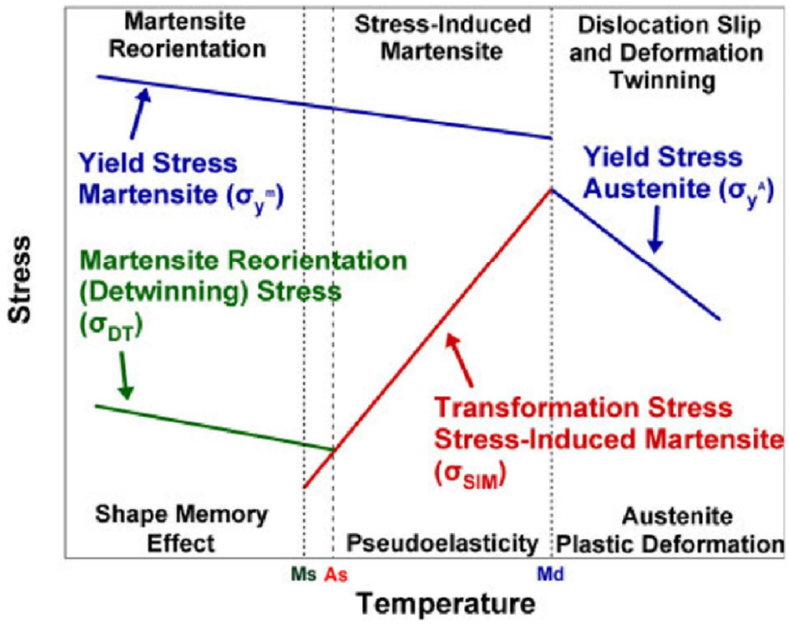

Figure 2.3: Typical behaviour of stress values [5]

alloys can produce high actuation strains, stresses and work outputs. Thus, SMAs can function as actuators, sensors or dampers, without the need for lubricants, complex assemblies or detailed inspecting or maintenance [3–5, 13]. For example, SMA-based solid state actuators can outperform pneumatic actuators and DC motors, while being smaller, lighter and considerably less complex [5, 13]. Moreover, SMAs may present good corrosion resistance, biological and magnetic resonance compatibility and high bending resistance, making them extremely fit for applications in the orthopaedic, orthodontic and neurosurgical fields [3].

The main SMAs systems are Fe-based, Cu-based and NiTi-based [2]. Among these, NiTi is the most studied one due to its structural practicality, significant work output, high strength, thermal and dimensional stability, high transformation strain and corrosion resistance, although it suffers from cyclic dimensional instability due to accumulation of irrecoverable

strain [2–4,6,7,14]. Hence, NiTi is the most used SMA in engineering, mainly in applications in the aerospace, automotive and biomedical (due to its high biocompatibility [15]) industries, as well as in power plants [16, 17]. Furthermore, it is used in everyday products like coffee machines, where it is employed as valves [11].

Nonetheless, some industries, mainly aerospace, require higher TTs and strength than what it is obtained from NiTi [2, 3, 5, 18, 19]. Thus, efforts have been made to elevate NiTi's transformation temperatures by controlling chemical composition and precipitates formation. Changes in composition also modify transformation strain and matrix strength [3]. Although it is possible to have TTs in NiTi up to 120 °C, in practice, stable phase transformation is limited to 100 °C [2–4, 6, 20].

2.3 Ni-Ti-Hf alloys

Any material that presents SME and SE above 100 °C is considered a high temperature shape memory alloy (HTSMA) [2,3,5,21,22] . These have been divided into three subcategories: groups I, II and III, associated with TTs in the ranges of 100 - 400 °C, 400 - 700 °C and $>$ 700 °C, respectively, although the number of available alloys that fit in groups II and III is very limited [5]. Due to the great characteristics of NiTi, having this alloy go through phase transformation at high temperatures would be ideal. One way to make NiTi a HTSMA is to alloy it with a third element [6,23]. Palladium (Pd), platinum (Pt), gold (Au), zirconium (Zr) and hafnium (Hf) have been tested with promising results, although the former three elements (Pd, Pt, Au) are too costly when compared to the remaining two and Zr is generally less stable than Hafnium. Furthermore, Zr presents an inferior shape memory behaviour

and has high oxygen affinity [2–6,13,18–20,22,24–27]. Additionally, Hafnium is more effective at altering TTs than any of the other ternary alloys making NiTiHf arguably the best HTSMA [5, 6]. It has been found that TTs in NiTiHf can occur in the range from -170 to 500 °C [6].

Variable geometry in the exhaust outlet case of jet engines (where the mixture of exhaust gases and fresh air is need to reduce noise during take-off but it is disadvantageous at cruising speed, as it reduces efficiency), clearance of the intake case relative to the blade tips in jet engines (which needs to be as small as possible for efficiency sake and thus needs to be compensated for heat expansion factors), valves with strict dimensional requirements in microelectromechanical systems (MEMS) applications and highly precise pressure transducers are just a few examples of HTSMA applications [5].

NiTiHf is arguably the most promising HTSMA due to its shape memory effect under high stress (above 500 MPa), excellent mechanical properties and dimensional stability, low cost and high work output [2, 3, 13, 28]. Additionally, it has been found to present TWSME after appropriate thermomechanical training [29]. However, it is usually associated with poor workability, low ductility, poor cyclic stability and high slope in the stress induced martensite transformation region and it is sensible to slight variations in its composition. Ageing treatments have a remarkable influence on its behaviour [2,3,5]. This alloy is pointed to work in the 100 - 300 °C range [3]. Nonetheless, the study of NiTiHf-based systems is still in its early stages [3].

When in its parent phase (austenite), NiTiHf is cubic B2, while martensite may present one of two crystal structures, depending on Hf content. Below 20 at.%, it is monoclinic B19' and it is orthorhombic B19 for higher concentrations (20-25 at.%) [5].

Increasing Ni content in NiTiHf (keeping Hf quantity constant and re-

ducing Ti), TTs remain constant up to a certain value, above which TTs decrease steeply. For low Hf content (up to 25 at.%), such value is roughly 50 at.% Ni, while for higher Hf percentages, this value tends to increase. On the other hand, the higher the Hf content, the steeper the decrease in TTs, as can be seen in Figure 2.4 [6]. It is important to note that some authors use M_s to represent the behaviour of TTs while others use M_p, the temperature value at which the forward transformation reaches its peak. In this study, it is considered that M_s and M_p follow the overall behaviour of TTs, which is a reasonable assumption. For example, at a 10 at.% Hf concentration, TTs are constant as Ni content increases up to around 50 at.% Ni, followed by an abrupt decrease [3], which behaviour is similar to that of NiTi [7].

Similarly, the effect of Hf content (keeping the Ni percentage constant) has been studied [6], varying Hf between 0 and 30 at.% and Ni content between 49.8 and 51.2 at.%, as shown in Figure 2.5. For a range from 0 to 10 at.% Hf, TTs (represented by M_s) were almost constant, although there is a slight tendency for a reduction in TTs, as Hf increases up to 10 at.%, specially for higher Ni concentrations (within the aforementioned range) [3, 5, 6]. For Hf content above 10 at .%, TTs increase continuously for all Ni concentrations. It is interesting to note that alloys with low Ni content (51.2 at.%, for example) show no martensitic transformation for a range Hf contents where a minimum would be expected [6].

In theory, Hafnium should be able to replace either Ni or Ti with equal preference, but in practice when Nickel is replaced with Hf, the latter will replace Ti instead, as Ni is depleted to form $(Ti,Hf)_2Ni$ phase precipitates [5]. Hence, Hafnium is always added at the expense of Titanium.

Although presenting high transformation temperatures, Ni-lean NiTiHf (i.e. Nickel content below 50 %) is seldom used mainly due to low strength

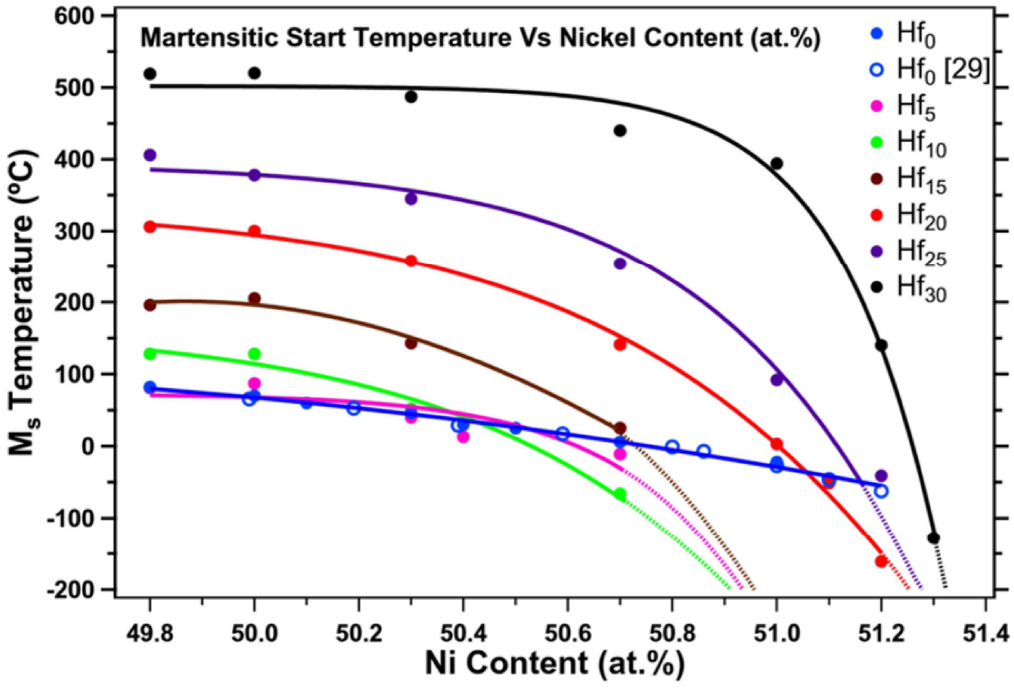

Figure 2.4: M_s dependency on Ni content [6]

for slip, unstable TTs during thermal cycling, absence of cyclic stability, large thermal hysteresis, reduced ductility at room temperature, unstable shape memory response and poor formability [3–5]. Moreover, Ni-lean NiTiHf lacks a stress plateau during martensitic phase transformation and does not present superelasticity. These have been attributed to dislocation slip occurring simultaneously with the occurrence of stress induced martensite, although these phenomena have been reduced or even eliminated upon precipitation strengthening [3].

Two-way shape memory effect has been observed in Ni-lean NiTiHf alloys [3,5]. In opposition, Ni-rich NiTiHf (Nickel content above 50 %) has been found to have high TTs, nearly perfect dimensional stability under compressive stress (500 MPa) and perfect superelasticity when properly heat-treated. Furthermore, Ni-rich NiTiHf may exhibit high yield strength at high temper-

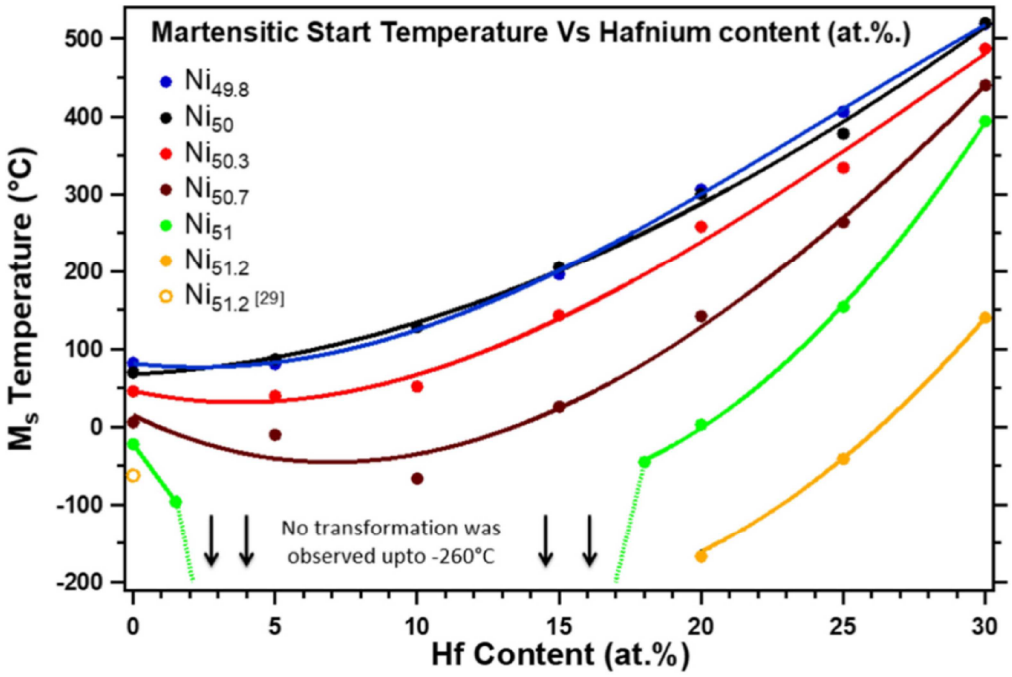

Figure 2.5: M_s dependency on Hf content [6]

atures [3, 4]. In its turn, increase in Hf content may lead to higher brittleness and more precipitate volume fractions [5].

Control over the microstructure of NiTi-based alloys (including NiTiHf) is crucial for tailoring its properties, manly those related to SME and SE, particularly precipitate size, interparticle distance and martensite morphology [3]. The latter has been found to be of one of two types: spear-like and mosaic-like. Grain size is also an important factor as grain refinement has been proven to strengthen Ni-lean NiTiHf [5].

NiTiHf easily forms precipitates. HfNi(Ti), Ti_2Ni(Hf), Hf_2Ni(Ti) have been found in Ni-lean NiTiHf. Furthermore, Ti_2Ni(Hf), either combined with HfNi(Ti) or not, limits the reversible phase transformation for Ni contents above 40 at.% and Hf below 30 at.% [3]. Among these, fine Ti_2Ni(Hf) (20 - 40 nm) plays an important role because it strengthens the matrix, eliminates

plastic deformation and enhances the SME and SE properties. $Ti_2Ni(Hf)$ concentrations decreases as Ni content increases. The size of $Ti_2Ni(Hf)$ precipitates is crucial as large precipitates (around 150 nm) reduce the matrix strength which results in incomplete shape recovery. These precipitates can be formed by annealing the alloy at 700 °C while the fine $Ti_2Ni(Hf)$ were the result of annealing at 500 °C [3]. Hence controlling martensite morphology requires control over the size of $Ti_2Ni(Hf)$ precipitates particles.

On the other hand, depending on composition and heat treatments, Ni-rich NiTiHf may either form $Ni_4(Ti, Hf)_3$ or a finely dispersed nanometre size precipitate, usually spindle-like, named *H-phase* which has a face-centred orthorhombic structure [30]. Without a unique composition [30] and formed upon ageing treatments in slightly Ni-rich NiTiHf containing 15 to 20 at.% Hf, these precipitates improve SME and SE properties due to precipitation strengthening [3, 4]. Compared to the alloy's matrix, H-phase precipitates are richer in Ni and Hf and leaner in Ti [4]. Furthermore, it increases TTs, enhances mechanical and functional properties, along with dimensional and thermal stability, limits residual strain during thermomechanical loading and offers high resistance to dislocation slip while allowing for the phase transformation to occur [2–4]. H-phase appears upon ageing treatments and it grows faster in alloys with higher Ni content since it depletes Ni form the matrix, making the precipitates themselves rich in Ni, while for a fixed Ni concentration, H-phases grows faster for higher Hf concentrations [3, 4, 18]. Decreasing the Ni content tends to increase TTs, thus it would be expected for H-phase to elevate TTs as it depletes Ni from the alloy's matrix [4].

The important factors to be controlled in order to obtain good SME and SE properties are particle size and interparticle distance. These are affected by the parameters of the ageing treatment, i.e. temperature and time. When

aged at 550 °C for 3 h the result is fine coherent precipitates particles (under 20 nm in length), while at 650 °C (for 3 h) the interparticle distance grows along with particle size (to 40 - 60 nm in length) which result in poor SME and SE properties [3,4]. A possible explanation is that martensite plates can include the precipitates during growth if these are small (result of ageing at 550 °C). On the other hand, these plates can grow between the precipitates if these are large and far apart, effectively controlling the thickness of the plates [3].

Quaternary NiTiHf systems have also been studied. NiTiHfPd presented high work output, strength and damping capacities and perfect superelasticity at the expense of increased brittleness and reduced TTs. Alloying Nb with NiTiHf resulted in a soft β phase which improved cold workability, which is one of the main NiTiHf flaws. Furthermore, Nb increases transformation strain, but reduces strength and TTs. While presenting two way shape memory effect and improving glass forming capability and thermal stability, NiTiHfCu reduced TTs [3].

As previously mentioned, control over precipitates formation and size is crucial to govern the properties of SMAs. Unlike large precipitates (several hundreds of nm) which have great thermomechanical fatigue life, small precipitates are able to be absorbed in the martensitic variants while keeping from disturbing the martensite phase motion front [4]. Thus, large precipitates present lower strength against dislocation plasticity resulting in poor shape memory recovery and large irrecoverable strains when compared to small precipitates [4]. Furthermore, large precipitates seem to result in transgranular fracture accompanied by large and sparse superficial cracks, while small precipitates favour a combination of transgranular and intergranular fracture along with small, dense cracks [4]. Hence, it is clear that a balance

between small and large precipitates is crucial. Ni-rich $Ni_{50.3}Ti_{29.7}Hf_{20}$ (at.%) aged for 3 h at 550 °C (as used in this study) has been pointed as exhibiting superior performance for actuation applications when compared to differently heat-treated $Ni_{50.3}Ti_{29.7}Hf_{20}$ (at.%) [4].

2.4 Tungsten inert gas welding

Tungsten inert gas (TIG, also known as GTAW - *gas tungsten arc welding*) is thought to have been first used in the United States of America (USA) around 1940 as a method to weld aluminium, a rather challenging process [31, 32]. About one decade later, TIG welding was introduced in Europe and in the United Kingdom (UK), where Argon was used instead of Helium (rare and expensive in Europe) as a shielding gas. The latter was used in the USA due to its abundant availability [31].

Being an electric arc process, TIG welding relies on electric current flowing from a tungsten electrode to the work-piece (i.e. the material to be welded) [33], covering the gap between these two and forming the electric arc, which results in a large quantity of heat being delivered to the work-piece with considerable control and precision [34,35], thus locally melting it. The melted material (weld pool) and its high temperature surroundings easily oxidise, requiring protective atmosphere, created by an inert gas, usually Helium or Argon. The shielding gas also serve secondary functions as will be discussed later.

Initially, the arc needs to be established by creating physical contact between the electrode and the work-piece, between which a high voltage drop has been imposed. This effectively shortens the circuit, increasing the electric current intensity. Hereupon, the two must be separated and the

consequent gap kept constant, creating the electric arc, which is stable even for low welding currents [36]. Due to the difficulty level associated with this process, a high frequency based process has been developed, eliminating the need to touch the work-piece with the electrode, thus aiding the welder in establishing the arc [37].

The voltage drop needed to create and maintain the arc is imposed by an *inverter* which allows its operator (the welder) to control welding parameters, mainly welding current. Often, direct current (DC) is used, where the electrode is connected to the negative terminal, making electrons leave the tungsten electrode and flow toward the workpiece, which is connected to the positive terminal [38]. This polarity, shown in Figure 2.6(a), is known as *direct current electrode negative* (DCEN) or *straight* or *direct* polarity. Due to the flow of electrons, heat distribution is roughly 1/3 and 2/3 for the negative and positive terminal, respectively [38], making DCEN deliver more energy to the work-piece than to the electrode.

Additionally, it is possible to use reverse polarity, where the electrode is connected to the positive terminal, making the electrons flow from the work-piece and against the electrode, delivering more heat to the latter, thus potentially requiring electrode cooling. This polarity, also known as *direct current electrode positive* (DCEP), is necessary when welding reactive materials such as Aluminium and Magnesium [38]. The electric arc ionises its surrounding gas, forming large positive ions that flow against the workpiece (negative terminal) and break the superficial oxide layer (alumina in the case of aluminium) [38], which present the main obstacle in welding these materials. Nonetheless, DCEP polarity is not without disadvantages as it may over-heat the electrode and result in shallow weld beads.

During the early stages of the TIG welding technology, alternated current

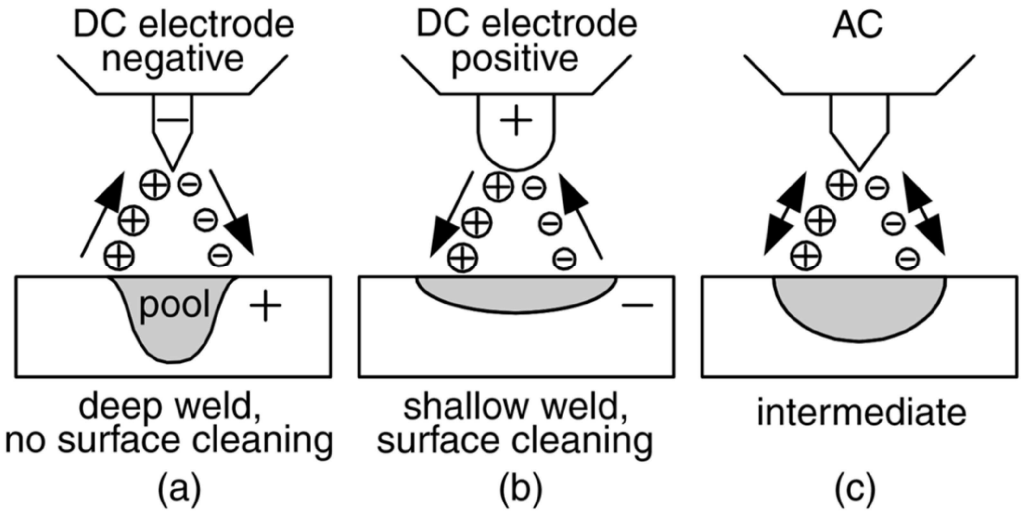

Figure 2.6: TIG welding polarities [38]

(AC) was used, which was associated with a number of problems, namely the *rectifier effect* that created a DC component and resulted in unclean welds [31]. The electric arc was responsible for this effect. Different solutions were found in the USA, where high voltage and high frequency were used (which were somewhat effective), and in the UK, where large capacitors were employed, considerably reducing the DC component. Yet, both methods resulted in radio frequency that heavily interfered with electronics such as computers [31, 37]. Such interference is still a problem today, albeit less severe due to developments in electronics. Nonetheless, TIG welding in AC mode presents the main advantages of DCEP and DCEN since it is able to remove the superficial oxide layer (without electrode overheating) and offers good penetration.

Shielding gas is mainly used to avoid oxidation and, additionally, help initiating and maintaining the arc, due to ionisation. While many gases are available and effective, Argon and Helium are the most common ones, among which Argon is fairly cost-accessible and requires less energy to ionise than

Helium, thus being considered the best by many [38].

As the name implies, TIG welding effectively requires tungsten[2] electrodes which may be alloyed to rare metal oxides (rarely above 4 %), usually Thorium dioxide (ThO_2). The electrode, considered non-consumable as it does not melt [39], is typically 1 to 2 mm in diameter and requires a sharp pointy tip to facilitate electron ejection. This tip may become dull overtime, due to oxidation and high temperatures, and require sharpening which results in electrode wear. It is good practice to have the tip well sharpened, preferably with the strains parallel to the axis of the electrode. If needed, zirconium, thorium, lanthanum and cerium, alloyed to tungsten, improve arc striking and stability as well as tip retention [31]. While the three latter alloys do not differ considerably amongst each other, zirconium and pure Tungsten are considered the most suitable for AC mode TIG welding.

Since it relies on a non-consumable electrode, TIG welding can be used for autogenous welds, i.e. no external material is added to the workpiece. Nonetheless, filler material may be used, where a rod is continuously fed to the weld pool. The quantity of added material is mostly independent from the welding current and speed, which may be advantageous when compared to other similar welding processes, such as MIG/MAG welding.

TIG welding produces clean, neat and compact weld beads, resulting in relatively small heat affected zone (HAZ) and good strength and penetration, as long as the welding parameters are correct. Typically, TIG welding happens in conduction mode (surface melting [38]). Cost effectiveness, precision and versatility (i.e. many metals can be welded in many different modes) make TIG welding a highly valuable process. Nonetheless, it is not without some flaws, namely the reduced productivity due to slow welding speeds, the

[2]Tungsten melting point: 3370 ^{o}C

need for highly experienced welders and the risk of having brittle weld beads if tungsten inclusions contaminate the weld pool.

3

Experimental procedure

Being a HTSMA, the NiTiHf alloy presents superelasticity and shape memory effects, which rely on the reversible martensitic transformation. SME occurs within a temperature range, defined by several factors, such as composition and precipitates. These two factors are related to each other in that, upon formation, precipitates can deplete elements from the matrix, thus altering transformation temperatures. Moreover, precipitates may present obstacles to the transformation, further affecting it. Consequently, the NiTiHf alloy is highly sensitive to any changes in these two factors, making the welding cycle potentially destructive to the functional properties of the alloy.

Although NiTiHf is considered resistant to oxidation, good gas shielding is crucial, since the high temperatures necessary to welding may promote material oxidation.

NiTiHf has been successfully laser welded (in keyhole mode[1]) [2], partly due to the highly controllable and localized heat delivery that is characteristic of laser welding. TIG welding shares these qualities, albeit on a smaller scale, thus indicating that sound TIG welds should be possible in NiTiHf.

Furthermore, TIG welding has been used in the NiTi alloy with excellent results [40].

As it happens with any scientific research procedure, processes and results need to be repeatable to guarantee that all parameters have been taken into account. To accomplished this, and decrease human error, an automated prototype was designed and built.

The objective of the prototype is to orbitally weld a 5 mm diameter rod with variable length (around 60 mm), as shown in Figure 3.1. The material of the rod is $Ni_{50.3}Ti_{29.7}Hf_{20}$ (at.%). Each weld should be performed in one single rod (effectively melting the material and consequently letting it solidify) and any given rod may be subjected to various welds. Considering that the most interesting properties of the alloy result from its unique composition, no material should be added, making the weld autogenous[2]. [41]

The prototype needs to reliably weld with negligible variations, thus all parameters must be controllable, namely *welding current*, *gas flow*, *welding time* and *welding speed*. *Arc gap* must be kept constant at a reasonable value.

3.1 Prototype design

A *Telwin Technology TIG 182* inverter was used, together with a manual a torch, which was secured in place by a simple structure composed of *Bosch aluminium profiles*, such that the torch could be adjusted in any way necessary and tightly fastened in place, as shown in Figures 3.2 and 3.3.

Secured by that same structure were the *stepping motors* which could be adjusted along the axial direction. These motors were responsible for the rotation of the rods, hence controlling welding speed.

[1]Keyhole: hole formed by concentrated heat that penetrates the workpiece. [41]

[2]Autogenous weld: A fusion weld made without the addition of filler metal.

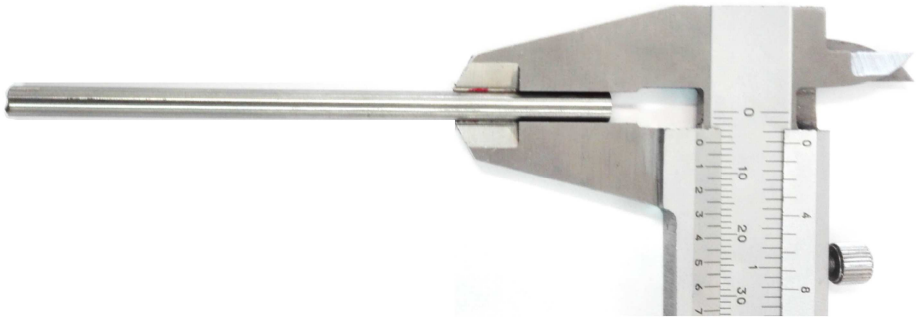

Figure 3.1: NiTiHf rod before welding

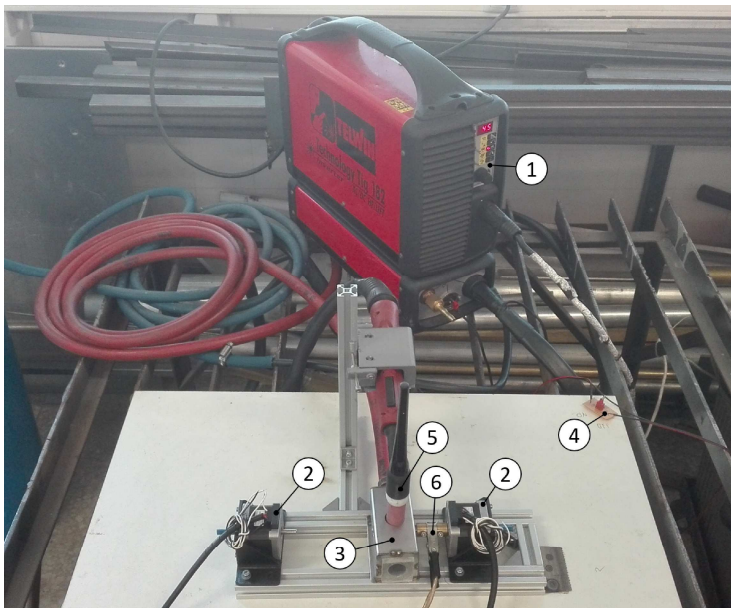

1. TIG weld inverter; 2. Stepping motors; 3. Gas container; 4. ON/OFF switch; 5. TIG weld manual torch; 6. Return (ground) cable

Figure 3.2: Welding prototype

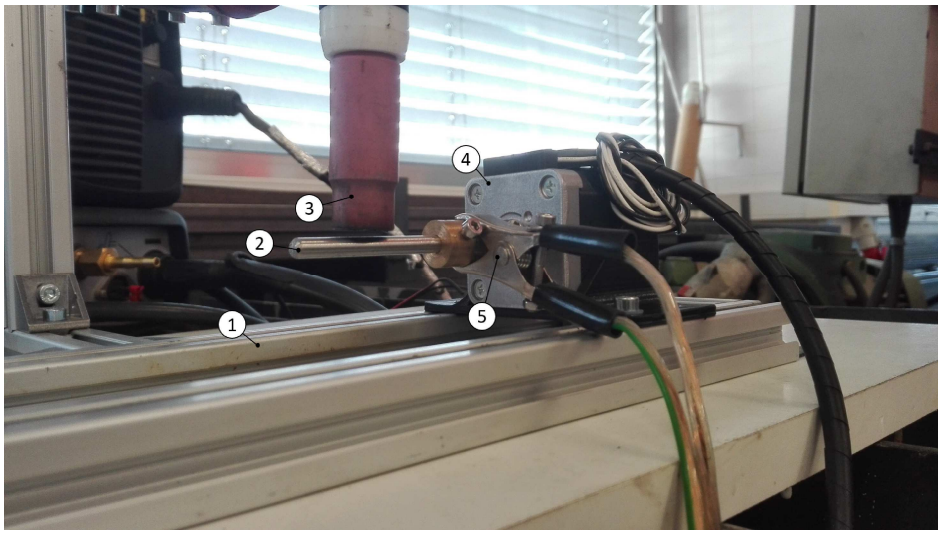

1. Aluminium structure; 2. NiTiHf rod; 3. Manual TIG torch nozzle; 4. Stepping motor; 5. Return (ground) cable clamp

Figure 3.3: Welding prototype without the gas container

The stepper motors were controlled by a *PiBot stepper driver*, connected to (a) an analogue wave generator that controlled the motor's speed, (b) a DC power source and (c) a National Instruments USB board which controlled the start and stop action of the motors (Figure 3.4).

The NI USB board was connected to a personal computer (PC) running *LabView* software. A routine was created which went through the welding cycles, each of which concluded with a new file where all the parameters were recorded. Additionally, the board commanded the inverter to start or cease welding.

The gas flow valve was fully open during welding and was operated manually so that pre-[3] and post-purge[4] times were not limited by the inverter. Visual and sonic signals were emitted by the PC, as part of the LabView

[3]Pre-purge: flow of shielding gas commences before the arc is struck [31]

[4]Post-purge: shielding gas continues to flow after the arc is extinguished [31]

routine, to aid the operator as to when to open or close the valve.

A second gas outlet was used to prevent oxidation (similar to a *back purge*[5]), along with a gas container, as shown in Figure 3.2.

3.2 Welding procedure

Before welding the NiTiHf rods and attending the alloy's high cost, stainless steel rods (316L, with a 5 mm diameter) were welded to find a good set of initial parameters. These welds were prepared and analysed through optical microscopy to confirm full penetration or lack thereof.

Each cycle went as follows: previously cut rods (using a precision cutting machine) were thoroughly cleaned with ethanol (96 % in volume) and dried out using compressed air. Being careful not to contaminate the rods, these were put in position, where the torch and gas container were previously set. Additionally, the arc gap was set using a thin metal sheet to guarantee that its value did not vary between any two welds. At this point, the *LabView* routine was initiated, which counted the time for pre-purge, followed by the welding time and finally the time for post-purge. Welding time was calculated so that one revolution was done during welding and pre- and post-purge times were determined empirically. Welding duration was 130 % of the calculated time to compensate for the lag in arc initiation, thus making sure the weld covers at least 360 °.

A welded rod can be seen in Figure 3.5.

Upon welding, it was noted that the alloy easily melted and dropped off which is an indication that heat does not flow easily within the alloy (i.e. low thermal conductivity). A clearly visible shadow covered up the weld bead as

[5]Back purge: additional shielding gas is piped to the underside of the weld bead [31]

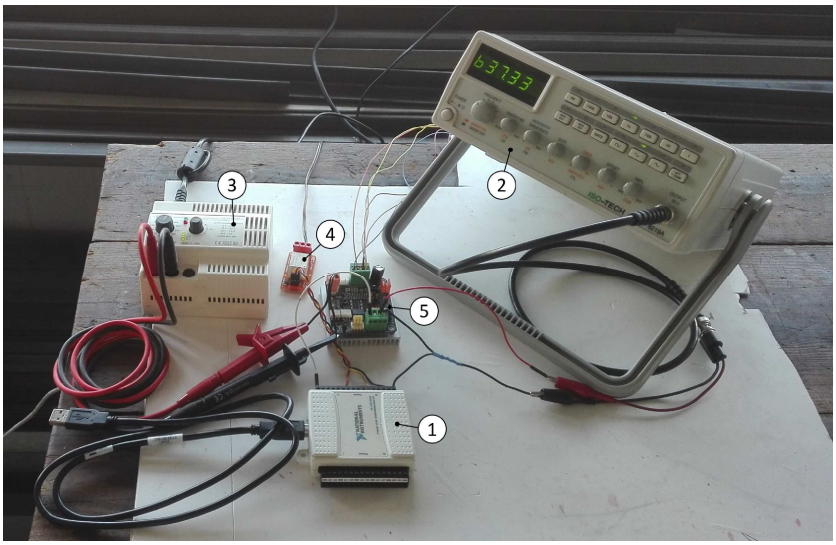

1. NI USB-6008 board; 2. Wave generator; 3. DC power supply; 4. Electromechanical relay; 5. Stepping motors' driver

Figure 3.4: Control devices of the welding prototype

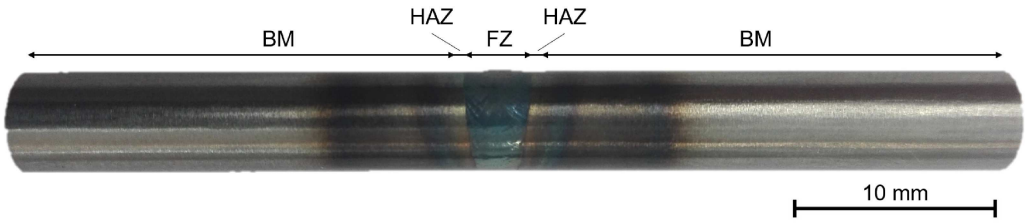

Figure 3.5: Welded NiTiHf rod

soon as the protective gas flow ceased, even after 10 s of post-purge. Considering that the alloy does not oxidise easily at room temperature, this effect must have been caused by the high temperature present in the surrounding area of the weld bead, contributing to thesis that the thermal conductivity is low.

3.3 Welding parameters

In order to study the influence of geometry in the optimal welding parameters, different length rods were welded, which were 49, 51 or 60 mm (shown in Figure 3.1).

Some parameters led to over-melting of the material and consequent dropping off, leaving a bulb of solidified material, which had to be ground. To make the best use of the limited available material, the ground rods (thus less than 60 mm in length) were still used for further welding.

Welding parameters used are presented in Table 3.1. The optimal set of parameters for the 60 mm rods resulted in over-melting when applied to the 51 mm ones. The reduction in length by 9 mm (15 %) may have been enough to prevent heat from flowing away from the bead, thus resulting in higher than ideal temperatures and consequent over-melting. Furthermore, comparing welds 2.2 and 3.3 in Table 3.1, one resulted in full penetration and the other in over-melting, respectively, further consolidating the hypothesis that heat flow is of great importance when welding the NiTiHf alloy.

Table 3.1: Welding parameters of the NiTiHf rods

Weld ID	Length [mm]	Welding current [A]	Welding speed [RPM]	Welding time [s]	Pre-purge [s]
1.1	60	45	10	9.20	6
1.2	<60	40	10	9.20	8
2.2	<60	35	12	6.50	8
2.4	<60	35	8	9.75	10
3.1	60	35	14	5.60	10
3.2	60	35	10	7.80	10
3.3	60	35	12	6.50	10
4.1	51	35	10	7.80	10
4.2	51	35	12	6.50	10
5.1	49	35	12	6.50	10

All welds had 20 s of post-purge and 12 l/min of gas flow.

3.4 Sample preparation and characterisation

Since weld 3.2 (in Table 3.1) was visually acceptable, samples were prepared for testing. The rod was cut to an appropriate length (guaranteeing all three zones were included - fusion zone, heat affected zone and base material) and then cut axially in two halves, which were mounted in resin. One of these was heat-treated (HT) in a pre-heated oven at 550 °C for 3 h and air cooled, wrapped in tantalum foil to prevent oxidation, while the other was kept as-welded (AW). The planar surface was polished and etched (using HF + HNO_3 + H_2O - 1:4:5 for 5 - 10 s).

Two rods, 51 mm in length each, were welded, once per rod, in the middle, using same set of parameters used in weld 4.2.

4

Results and discussion

In order to characterise the welded NiTiHf alloy, several tests were performed, namely optical microscopy, scanning electron microscopy, the Vickers hardness test and differential scanning calorimetry, using the samples from the 60 mm rods (weld 3.2 presented in Table 3.1).

Additionally, mechanical testing was performed using the two 51 mm rods, which were welded using the set of parameters used in weld 4.2 (Table 3.1).

Defects in the base material (as-received) were found in some samples (shown in Figure 4.1), which should be accounted for when interpreting the results from each test, mainly the Vickers hardness test and mechanical testing.

4.1 Optical microscopy

Optical microscopy was performed to visually assess the physical integrity of the welds. The results are depicted in Figure 4.2 , where some areas of interest are presented in greater detail.

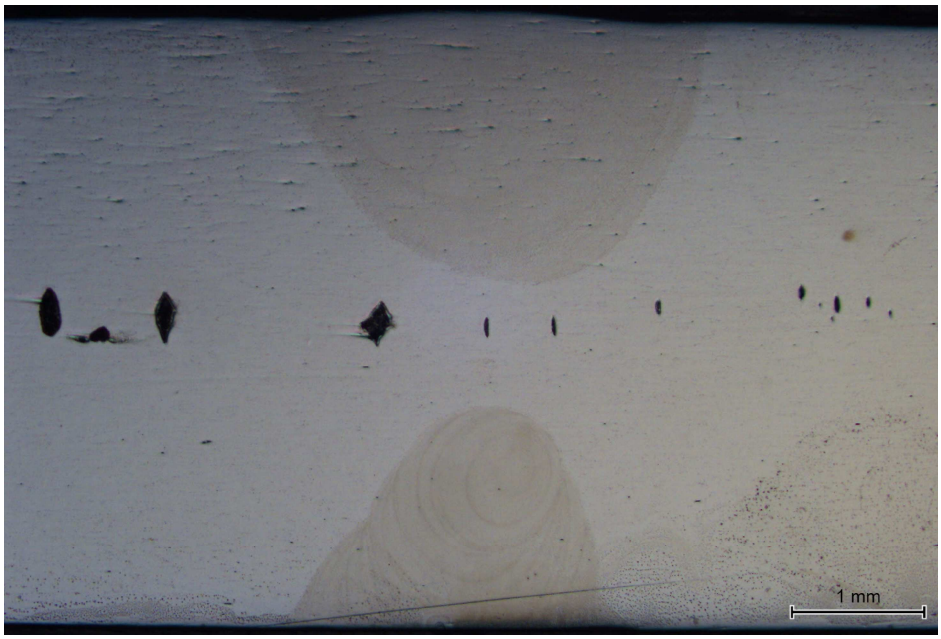

Figure 4.1: Defects present in the base material

The fusion zone (seen as the darkest area in Figure 4.2) is clearly visible due to its larger grain size compared to the base material (BM). Contrarily, the heat affected zone (HAZ) is not easily distinguishable from the BM, although slightly larger grain can be seen in Figure 4.2 (b. and d.). The interface between the fusion zone (FZ) and HAZ is depicted in detail in Figure 4.2b., where a dendritic network can be observed. Such network, which also existed when the alloy was laser welded [2], was likely caused by partial melting of the material [38].

It is interesting to note the well defined centreline in Figure 4.2e. which confirms a stable arc during the welding process.

In the root of the FZ, it is clear that the weld bead overlapped, as intended, resulting in refined grain that was likely caused upon the second passing of the arc, when the loosening of the grains that originated from the first passing became kernels for the growth of new, smaller grains [42].

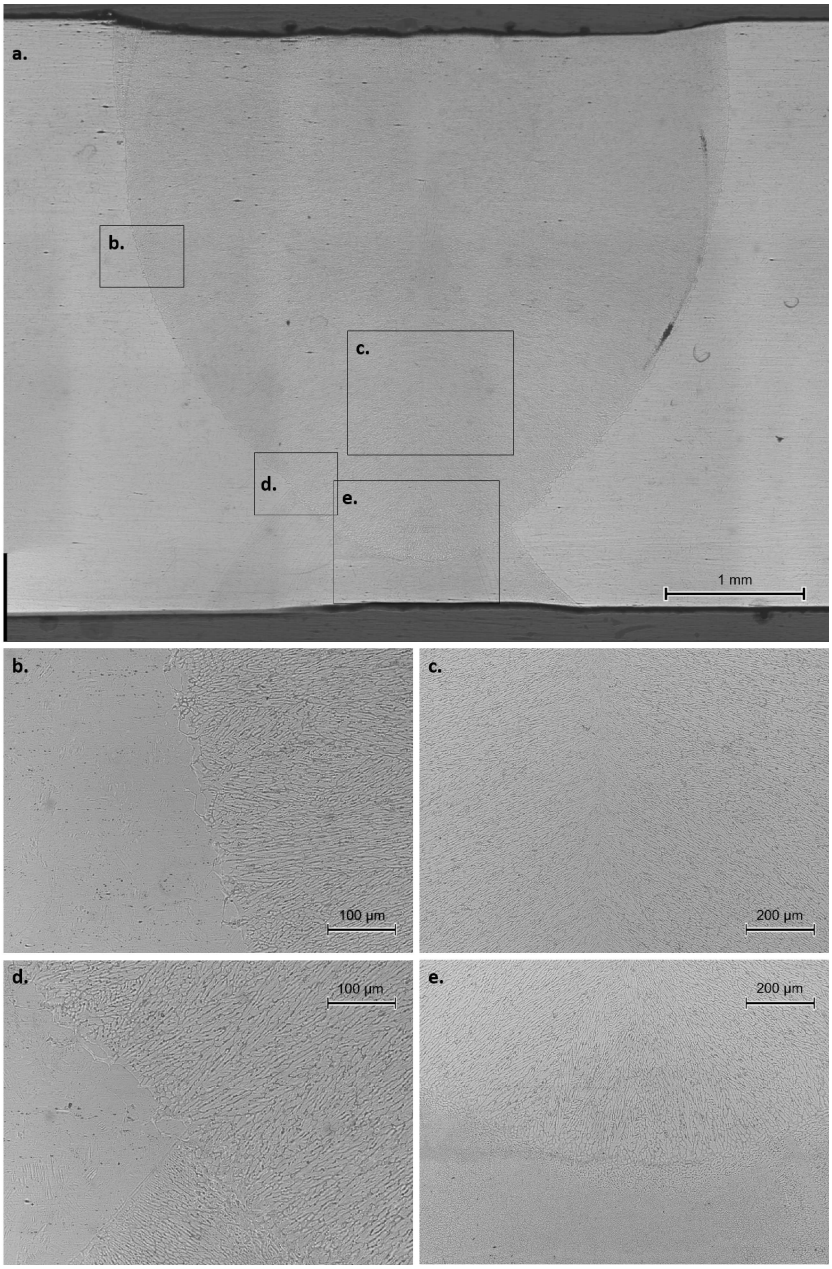

a. Complete view of the fusion zone; b. FZ/HAZ interface; c. Intersection between the HAZ, FZ and overlapped FZ; d. Refined grain; e. Weld bead centreline

Figure 4.2: Optical microscopy of the as-welded sample

Additionally, the overlapping created a triple interface zone, seen in Figure 4.2d., where both the smaller and larger grain meet each other as well as the HAZ.

Several welds were done in order to find the ideal set of welding parameters and it was clear that a small change in the quantity of energy delivered to each rod (either through altering welding current or speed) resulted in considerable changes in the amount of molten volume. Figure 4.2a. shows that penetration was deeper than ideal, since the fusion zone (coming from the top) goes well beyond the horizontal axis, while penetration at the bottom would not have been sufficient, as it does not reach the axis. The difference in penetration is most likely linked to the amount of energy delivered at any instance, i.e. at a given moment, at the beginning of the weld, the total energy that had been delivered was insufficient. Yet, due to the low heat flow (which leads to increased temperature), a thermal stationary state could not be attained thus resulting in an increasing volume of weld pool over time, increasing penetration beyond desirable. Although the weld bead shown in Figure 4.2 is visibly sound, it should be concluded that the NiTiHf alloy is susceptible to small variations in parameters, mainly those directly affecting energy delivery, such as welding current and speed.

As expected, considering the nature of TIG welding, the welds occurred in conduction mode, as opposed to keyhole mode that mainly occurs in Laser welding [2].

Figure 4.2 has a long, curved defect which was likely caused by random impurities contained in the material prior to welding, hence it should not be a systematic problem.

Furthermore, it should be noted that the diameter of the rod in the fusion zone was reduced, which indicates loss of material probably due to

evaporation.

4.2 SEM

Scanning electron microscopy (SEM), shown in Figures 4.3 and 4.4, was performed as a complementary test to optical microscopy (Section 4.1). Both figures are relative to the heat-treated samples. Accelerating voltage was 20.00 kV and the working distance ranged from 8.0 to 11.5 mm.

Figure 4.3 shows the difference in grain size between the fusion zone (top, right) and the heat affected zone (bottom, left), where grain is considerably larger in the former. Furthermore, a dendritic network can be seen in the interface between these two zones (FZ and HAZ), as it was observed in optical microscopy (Section 4.1). Additionally the dendritic network can be observed in Figure 4.4.

4.3 Vickers hardness test

The Vickers hardness test was performed in both the as-welded and the heat-treated samples so that the influence of the welding cycle and the heat-treatment on the alloy's hardness could be assessed. Both samples were indented with a load of 0.3 kg for 10 s over an area which included the fusion zone (including the centreline), the heat affected zone and the base material. Since the HAZ was not easily identifiable, the area was selected so that the BM would be undoubtedly included. The results are presented in Figures 4.5 and 4.6, where the weld centreline (as can be seen in Figure 4.2.c), FZ/HAZ interface and axis of the welded rod are indicated to facilitate figure interpretation. Figure 4.7 allows a comparison between the two samples.

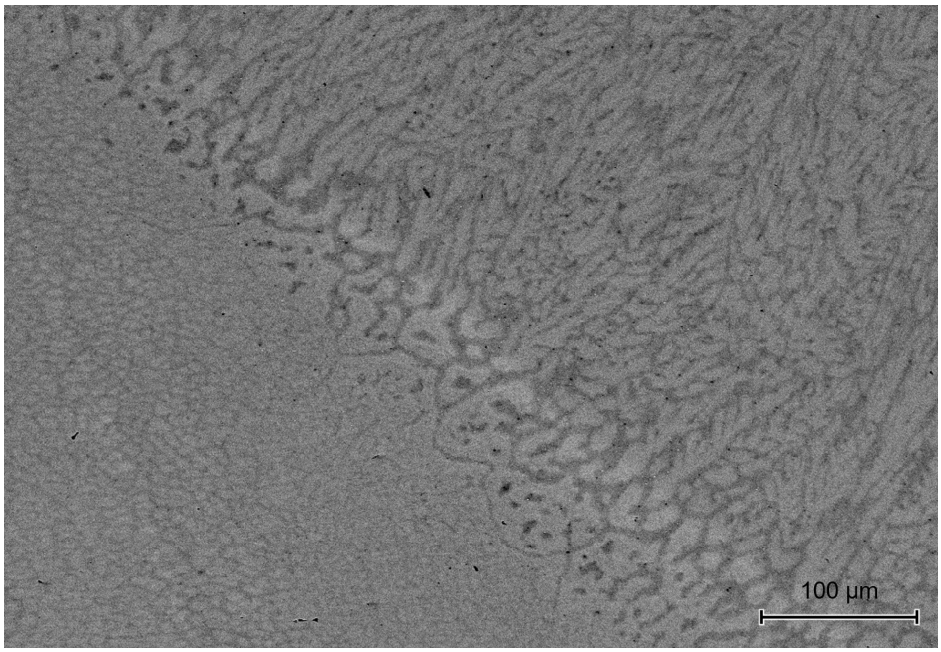

Figure 4.3: FZ/HAZ interface of the heat-treated sample (SEM)

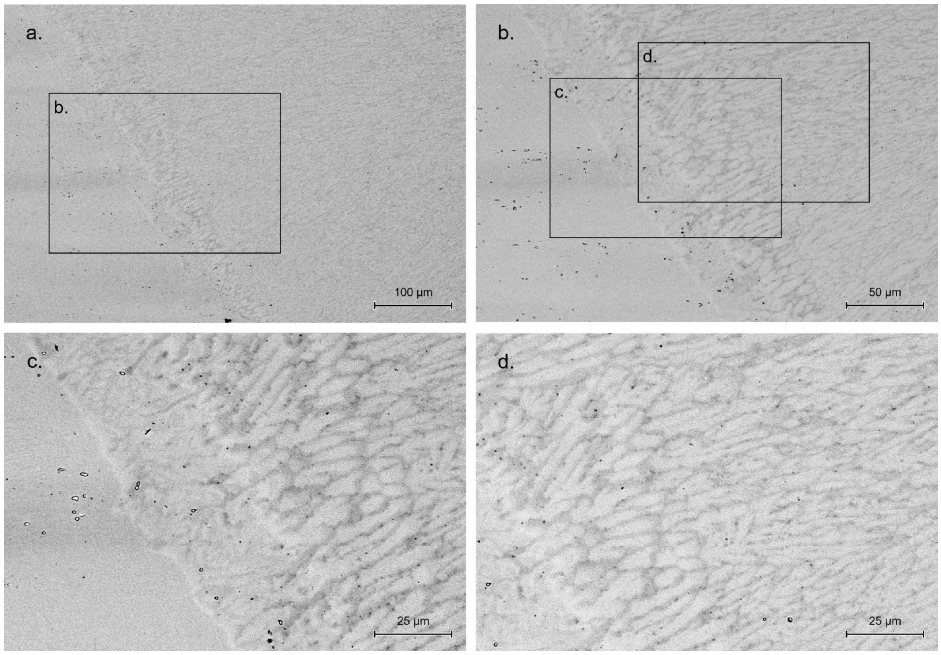

Figure 4.4: SEM of the heat-treated sample (with details)

To avoid the influence of other factors, every indentation was at least 0.250 mm from the sample's border. Indentations were separated from each other by 0.200 mm along the axial direction, totalling 12 mm, and 0.400 mm in the perpendicular direction, along the entire width of the sample.

Figure 4.5 clearly shows a difference in hardness values between the fusion zone (where mostly violet and dark blue are dominant) and the base material (where light green is mostly present). FZ averaged 384.5 HV and the BM, 405.7 HV. This difference is explained by the larger grains present in the FZ, which tends to decrease hardness values.

Consequently, the heat affected zone should present intermediate hardness compared to the FZ and BM. Indeed, it is possible to observe a small thin area close to the FZ/HAZ interface which follows its silhouette and presents average hardness values higher than the FZ and lower than the BM.

Furthermore, a few areas of interest can be seen in Figure 4.5 such as the soft area which coincides with the centreline of the fusion zone, while the refined grain (at the bottom of the FZ, seen in Figure 4.2.e) has slightly higher hardness values than most of the FZ.

The heat-treated sample presents considerably higher values than the as-

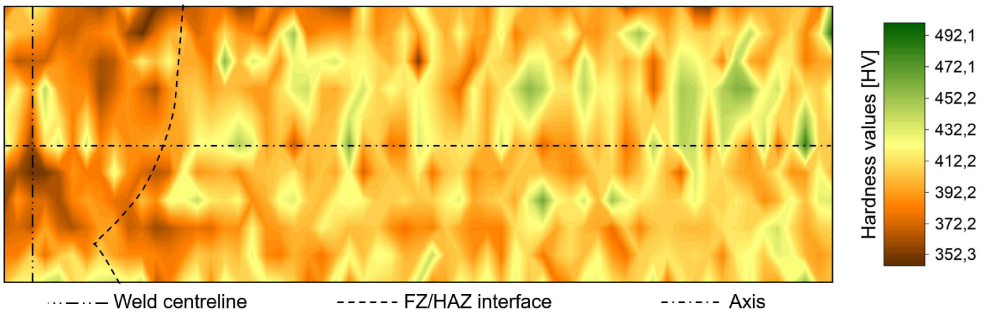

Figure 4.5: Hardness values of the as-welded sample

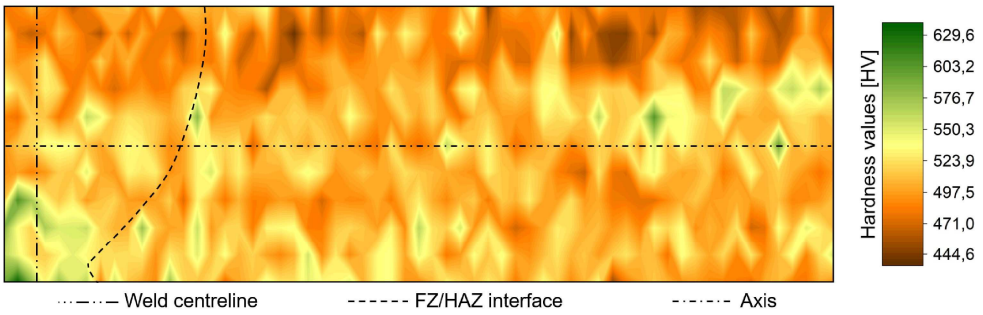

Figure 4.6: Hardness values of the heat-treated sample

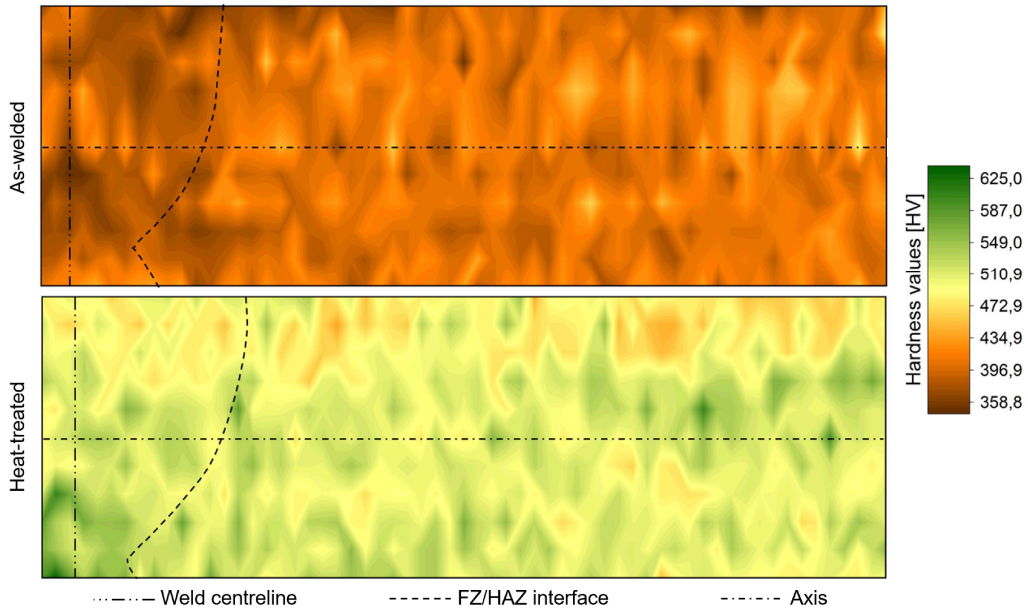

Figure 4.7: Hardness values of the AW and HT samples

welded sample. Heat-treatment promotes the growth of H-phase, which is known to increases hardness. The average hardness value (measured on what was the BM) is 502.8 HV. In Figure 4.6, the FZ, HAZ and BM zones are not as clearly identifiable as in Figure 4.5, since the growth of H-phase is homogeneous in the material. Nonetheless, this effect is balanced by the fact that grain size, which did not alter during heat-treatment, also affects hardness values, hence maintaining a slight difference in hardness values between the BM and FZ.

4.4 DSC

Differential scanning calorimetry (DSC) was performed on two samples, consisting of base material (BM) and fusion zone (FZ), both in as-welded condition, in order to evaluate transformation temperatures (TTs). Many practical applications of (HT)SMA rely on the martensitic transformation occurring within a well defined temperature range.

There are several methods to find transformation temperatures of shape memory alloys (including HTSMA). While some measure TTs directly, like electric resistivity, dilatometry (if the martensitic transformation leads to significant change in volume) and *in situ* X-ray, others provide data which correlates to these transformations, thus considered indirect [5]. One example of an indirect method is differential scanning calorimetry (DSC), where temperature variation is imposed on two volumes, heating or cooling at a steady rate. One of the volumes serves only as a reference, used to monitor the heat flow that is entering or leaving the sample (i.e. the second volume) [5]. Variations in heat flow identify endothermic or exothermic reactions, represented either as *peaks* or *valleys* on plotted data [5], depending on signal convention.

Hence, DSC is an expeditious way of identifying martensitic transformations, since the direct and reverse transformations are exothermic and endothermic, respectively.

DSC was performed on a 52.5 mg base material sample and on a 80.2 mg fusion zone sample, between -50 and 250 °C (both heating up and cooling down), since it was expected that transformations would occur within this range. The rate at which temperature varied was 10 °C/min.

The DSC data is plotted in Figures 4.8 and 4.9, relative to the base material and the fusion zone, respectively. Each figure shows two curves, one relative to the direct transformation (cooling) and one relative to the reverse transformation (heating).

Martensitic transformations are usually characterised by the transformations temperatures, determined through a simplification of the DSC curve [5] (hereafter called *nominal* curve). Observing any of the curves in Figures 4.8 and 4.9, it is clear that each one consists of two main parts: an horizontal line (baseline), that represents the heat flow for a single phase, and peak (or valley), which is related to phase transformation. A simplified curve should present both these features, where the single phase heat flow is represented by a straight line that coincides with the real baseline and two sloped straight lines which, combined, represent the peak or valley. Plotting the simplified curves (i.e. nominal curves, not represented) it is possible to find the nominal transformation temperatures, presented in Table 4.1. Note that M_p and A_p identify the temperatures at which the forward and reverse transformations reach their energy flow peak, respectively.

Transformation temperatures were found based on an energy criterion, i.e. should one transformation follow the nominal curve, its total energy must be equal to that of the real curve. It should be noted that the temperature was

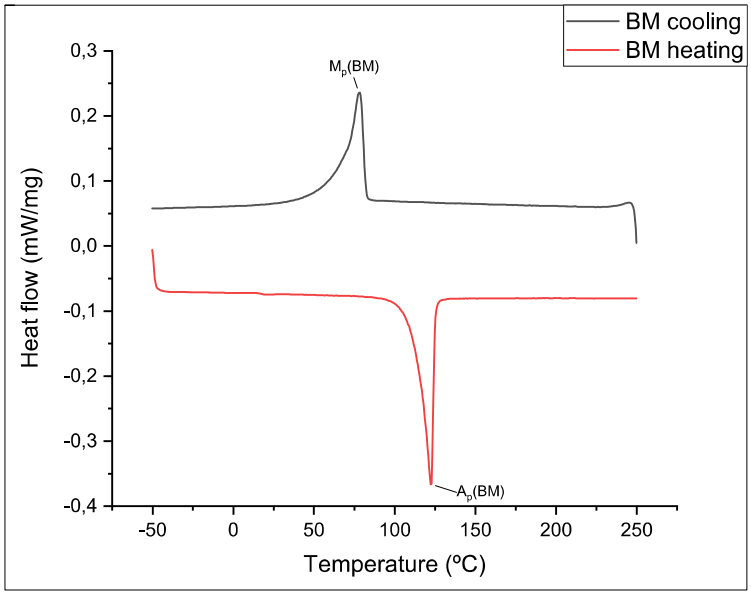

Figure 4.8: DSC curves of the base material sample

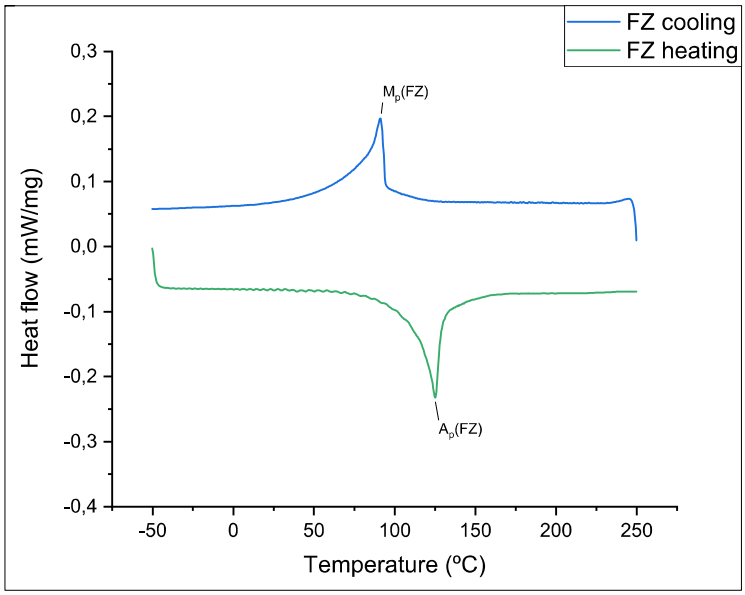

Figure 4.9: DSC curves of the fusion zone sample

Table 4.1: Nominal transformation temperatures

	M_s	M_p	M_f	A_s	A_p	A_f
BM (°C)	85.9	78.3	56.5	110.7	122.3	129.3
FZ (°C)	99.4	91.3	64.8	105.2	125.3	139.0
$diff$ (%)	15.7	16.6	14.7	5.0	2.5	7.5

$diff = (X_{BM} - X_{FZ}) * 100/X_{BM}$

increased or decreased at a constant rate (10 °C/min), and that the integral of any of the curves with respect to the temperature is proportional to the total energy associated with the respective transformation, since integrating the curve with respect to time gives the value of the total energy.

The curves show that heat flow is constant as long as the material presents one phase only, demonstrated by the almost perfectly horizontal baselines. The fact that the heat flow values associated with the baselines are roughly the same, both before and after each transformation and amongst all curves, signifies that the c_p value is a property of the material and not the phase.

Table 4.1 shows the nominal TTs values as well as the relative difference between the base material and fusion zone values. Regarding the reverse transformations, peak temperatures differ slightly, as does the temperature range within which transformation occurs, being wider for the FZ than for the BM. This widening may be due to the larger grain observed in the fusion zone, compared to the base material. However, these deviations are not significant. Contrarily, the direct transformations differ notably both in peak temperature and in temperature range, meaning that, for certain temperature values, a welded piece may be undergoing a martensitic transformation in the fusion zone while it is still a stable single phase in the base material.

Furthermore, the high temperatures reached during the welding cycle may lead to nickel evaporation due to its high vapour pressure, thus reducing Ni

content [43]. Consequently, considering TTs behaviour with variations in Ni content (Figure 2.4), transformation temperatures tend to increase, as was observed.

Comparing the base material to the fusion zone, it is interesting to note that the heat flow values at peak temperatures was reduced, while the temperature range widen, indicating that the total energy associated with each transformation may be roughly the same for both the BM and the FZ. In fact, there are only a 7.0 % and a 5.2 % differences in the total energy for the direct and the reverse transformations, respectively.

Values in Table 4.1 show that the alloy cannot be considered a HTSMA, since the forward transformation occurred below 100 °C, both in the fusion zone and the base material. Nonetheless, TTs can be increased above 100 °C through heat-treatment, as it will be concluded from mechanical testing (Section 4.5).

4.5 Mechanical testing

Two welded rods were thermally cycled once at a nominal constant stress value (isobaric load) in order to assess the mechanical behaviour of the welded NiTiHf alloy. One rod was tested in the as-welded condition and the other was heat-treated at 550 °C for 3 h prior to testing. The oven was pre-heated to 550 °C and the rod was air-cooled. Before testing, both rods were machined to 4 mm in diameter and 50 mm in length, as shown in Figure 4.10.

Using the apparatus shown in Figure 4.11, each rod was successively pre-loaded to a given stress value (50, 100, 200, 300, 400 MPa or until failure) at 50 °C and isobarically subjected to one thermal cycle (heating up to 300 °C

Figure 4.10: Machined rod

and cooling back to 50 °C) at each stress level. Maximum and minimum temperature values were selected to guarantee fully austenitic or martensitic phases, respectively. Strain values were measured using an extensometer.

The mechanical behaviour of both rods are depicted in Figure 4.12, from which transformation temperatures were calculated through a procedure similar to the one depicted in [44], as were the hysteresis and the work output values presented in Table 4.2. It should be noted that, being a graphical method, there is a low level of accuracy associated.

The as-welded rods presented negligible unrecoverable strain for each cycle, represented in Figure 4.12 as the vertical distance between the heating and cooling curves at low temperature, and relatively low thermal hysteresis (around 35 °C). Nonetheless, and despite the fact that work output values are reasonably good (compared to values found in literature, [45]), the as-welded NiTiHf cannot be considered a high temperature shape memory alloy, since transformation occurred at temperatures below 100 °C. Moreover, the rods failed at 400 MPa.

The heat-treated rods showed zero residual strain and a smaller thermal hysteresis (at around 22 °C), compared to the as-welded rod. Additionally, the considerably high work output values (although slightly lower than those produced by the as-welded rods) make them usable as HTSMA actuators for

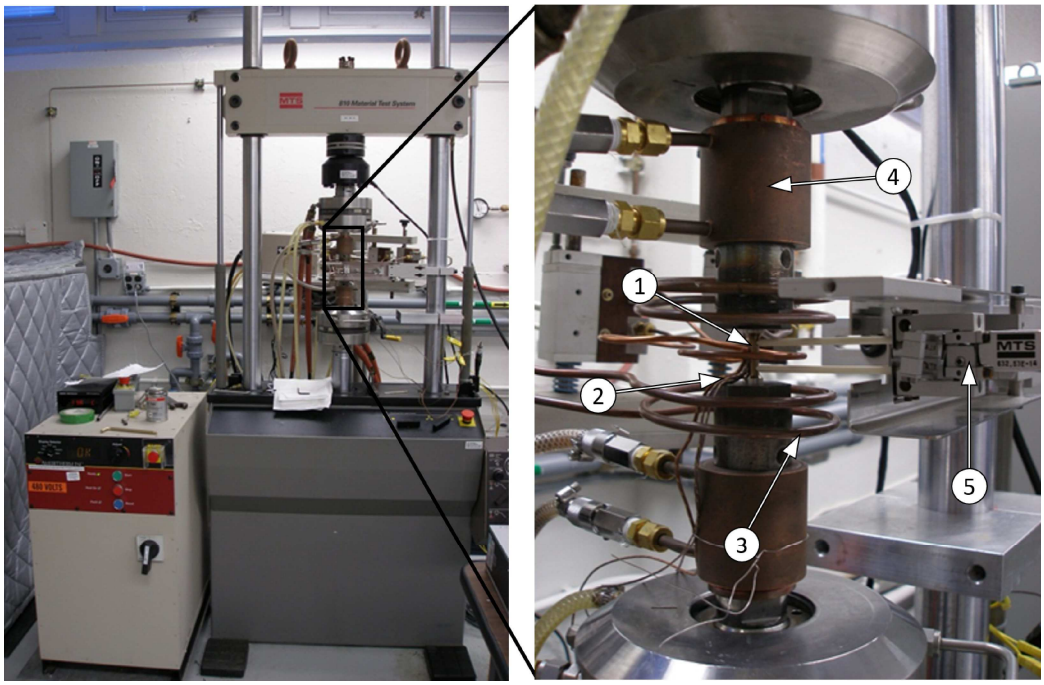

1. NiTiHf rod; 2. Thermocouples; 3. Induction coils; 4. Cooling jackets; 5. Extensometer

Figure 4.11: Mechanical testing equipment

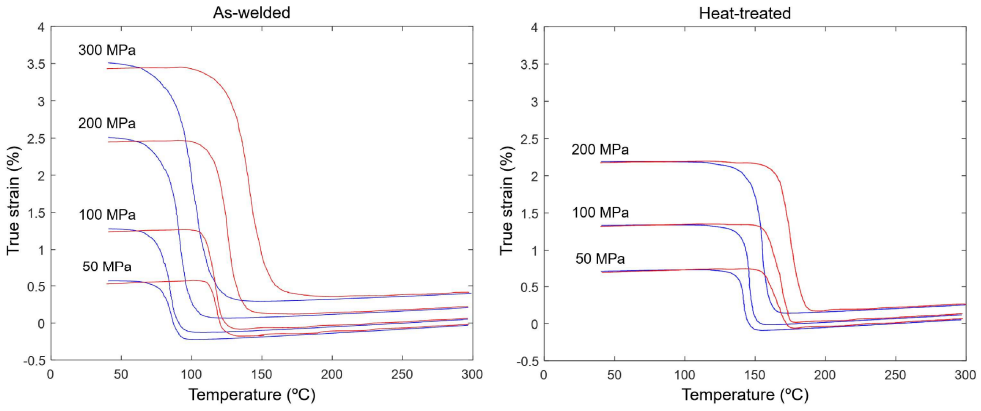

Figure 4.12: Thermal cycling at constant stress

Table 4.2: TTs, hysteresis and work output values

State when tested	Isobaric loading (MPa)	TTs				Hysteresis (°C)	Work output (J/cm^3)
		M_s (°C)	M_f (°C)	A_s (°C)	A_f (°C)		
AW	50	90	79	113	123	34	0.38
HT	50	145	139	156	174	24	0.40
AW	100	90	76	110	123	35	1.43
HT	100	149	142	159	175	22	1.34
AW	200	99	81	117	134	35	4.68
HT	200	160	149	167	183	20	4.06
AW	300	115	87	127	154	39	9.36

stresses equal to or below 200 MPa.

Reference values can be found in literature, where 0.70 J/cm^3 strain was attained by cycling Ni-rich NiTiHf isobarically at 100 MPa and M_s and A_f occurred at 120 and 155 °C, respectively. In the present work, the heat-treated welded NiTiHf rods presented higher work output and higher transformation temperatures. Furthermore, thermal hysteresis is reported to be roughly constant, at 35 °C (up to 700 MPa) [45], as was attained in this work. Hence, it may be considered that the welded rods have excellent mechanical properties up to 200 MPa.

Table 4.2 shows that transformation temperatures of the heat-treated rods are consistently higher compared to the as-welded ones. While the latter fail to present high temperature shape memory effect, heat-treated rods can effectively be employed as HTSMAs since both direct and reverse transformations happen above 100 °C.

Regarding hysteresis and work output, heat treatment did not considerably affect the alloy although a slight reduction in both parameters did occur. There is a slight trend for TTs to increase as isobaric loading increases, which behaviour has been documented in literature [13].

5

Conclusions

In this work, 5 mm diameter $Ni_{50.3}Ti_{29.7}Hf_{20}$ (at.%) rods, which length varied between 49 and 60 mm, were radially TIG welded with promising results, although further research is needed.

Tungsten inert gas welding technology is compatible with the alloy, i.e. arc was easy to initiate and stabilise and the shielding gas prevented oxidation during welding. Although a gas container with two inlets was used, it is possible that the quantity of gas flow typically used in TIG welding is sufficient. Furthermore, it was established that superficial oxidation is prone to happen while the alloy is at elevated temperatures, hence post-purge is crucial. Some commercial TIG welding equipment may have to be adapted in order to provide sufficient post-purge times.

It is possible that the thermal conductivity of the NiTiHf alloy (which value is still unknown) is low, since a thermal stationary equilibrium did not seem to have occurred, which would explain the sensitivity to small changes in welding parameters. Further evidence was found through optical microscopy, where penetration and bead width increased with welding distance. Furthermore, low power (low welding current and high welding speed) suffices to

weld the alloy and prevents over-melting.

Through DSC and mechanical testing, SME and SE were observed after welding and it was clear that heat treatment is crucial in obtaining TTs above 100 °C. Moreover, the welded rods showed great potential for applications as low stress solid state actuators (up to 200 MPa).

It should be noted that, due to the material high cost, 5 mm diameter rods were used in this study, which may not represent the majority of geometries and dimensions used in engineering, often subjected to welding.

For future research, a different geometry is advised and the study of the thermal behaviour of the alloy is suggested with the objective of attaining a stationary thermal state, for which a cooling system may be necessary.

Additionally, cyclic behaviour, isothermal curves and fracture analysis, which have not been performed in the present work, would give important information about the applicability of TIG welded NiTiHf rods as actuators.

Finally, H-phase presence and distribution should also be assessed, possibly through transmission electron microscopy (TEM).

Bibliography

[1] S. Preibisch, S. Saalfeld, and P. Tomancak, "Globally optimal stitching of tiled 3D microscopic image acquisitions," *Bioinformatics*, vol. 25, pp. 1463–1465, 04 2009.

[2] J. Oliveira, N. Schell, N. Zhou, L. Wood, and O. Benafan, "Laser welding of precipitation strengthened Ni-rich NiTiHf high temperature shape memory alloys: Microstructure and mechanical properties," *Materials & Design*, vol. 162, pp. 229 – 234, 2019.

[3] H. E. Karaca, E. Acar, H. Tobe, and S. M. Saghaian, "NiTiHf-based shape memory alloys," *Materials Science and Technology*, vol. 30, no. 13, pp. 1530–1544, 2014.

[4] O. Karakoc, C. Hayrettin, A. Evirgen, R. Santamarta, D. Canadinc, R. Wheeler, S. Wang, D. Lagoudas, and I. Karaman, "Role of microstructure on the actuation fatigue performance of Ni-Rich NiTiHf high temperature shape memory alloys," *Acta Materialia*, vol. 175, pp. 107 – 120, 2019.

[5] J. Ma, I. Karaman, and R. D. Noebe, "High temperature shape memory alloys," *International Materials Reviews*, vol. 55, no. 5, pp. 257–315, 2010.

[6] T. Umale, D. Salas, B. Tomes, R. Arroyave, and I. Karaman, "The effects of wide range of compositional changes on the martensitic transformation characteristics of NiTiHf shape memory alloys," *Scripta Materialia*, vol. 161, pp. 78 – 83, 2019.

[7] J. Oliveira, R. Miranda, and F. B. Fernandes, "Welding and joining of NiTi shape memory alloys: A review," *Progress in Materials Science*, vol. 88, pp. 412 – 466, 2017.

[8] J. Seo, Y. C. Kim, and J. W. Hu, "Pilot study for investigating the cyclic behavior of slit damper systems with recentering shape memory alloy (SMA) bending bars used for seismic restrainers," *Applied Sciences*, vol. 5, no. 3, pp. 187–208, 2015.

[9] B. Crispim, "Gas tungsten arc welding of Cu-Al-Mn shape memory alloys," Master's thesis, Faculdade de Ciências e Tecnologia - Universidade Nova de Lisboa, 2018.

[10] A. Evirgen, *Microstructural characterization and shape memory response of Ni-Rich NiTiHf and NiTiZr high temperature Shape Memory Alloys*. PhD thesis, Texas A&M University, 2014.

[11] J. Frenzel, E. George, A. Dlouhy, C. Somsen, M.-X. Wagner, and G. Eggeler, "Influence of Ni on martensitic phase transformations in NiTi shape memory alloys," *Acta Materialia*, vol. 58, no. 9, pp. 3444 – 3458, 2010.

[12] M. Schwartz, *Encyclopedia of Smart Materials*. John Wiley & Sons, Inc., 2002.

[13] O. Benafan, R. D. Noebe, S. A. Padula, and R. Vaidyanathan, "Microstructural response during isothermal and isobaric loading of

a precipitation-strengthened Ni-29.7Ti-20Hf high-temperature shape memory alloy," *Metallurgical and Materials Transactions A*, vol. 43, pp. 4539–4552, Dec 2012.

[14] G. S. Ded, "Characterization of Ni-rich NiTiHf based high temperature shape memory alloys," Master's thesis, University of Kentucky, 2010.

[15] N. Sharma, K. K. Jangra, and T. Raj, "Fabrication of NiTi alloy: A review," *Proceedings of the Institution of Mechanical Engineers, Part L: Journal of Materials: Design and Applications*, vol. 232, no. 3, pp. 250–269, 2018.

[16] J. Sam, B. Franco, J. Ma, I. Karaman, A. Elwany, and J. Mabe, "Tensile actuation response of additively manufactured nickel-titanium shape memory alloys," *Scripta Materialia*, vol. 146, pp. 164 – 168, 2018.

[17] M. Mehrpouya, A. Gisario, and M. Elahinia, "Laser welding of NiTi shape memory alloy: A review," *Journal of Manufacturing Processes*, vol. 31, pp. 162 – 186, 2018.

[18] O. Benafan, G. Bigelow, and D. Scheiman, "Transformation behavior in NiTi-20Hf shape memory alloys – transformation temperatures and hardness," *Scripta Materialia*, vol. 146, pp. 251 – 254, 2018.

[19] J. Rao, T. Roberts, K. Lawson, and J. Nicholls, "Nickel titanium and nickel titanium hafnium shape memory alloy thin films," *Surface and Coatings Technology*, vol. 204, no. 15, pp. 2331 – 2336, 2010.

[20] Y. Tong, Y. Liu, J. Miao, and L. Zhao, "Characterization of a nanocrystalline NiTiHf high temperature shape memory alloy thin film," *Scripta Materialia*, vol. 52, no. 10, pp. 983 – 987, 2005.

[21] D. C. Lagoudas, *Shape Memory Alloys.* Springer, 2008.

[22] M. Elahinia, N. S. Moghaddam, A. Amerinatanzi, S. Saedi, G. P. Toker, H. Karaca, G. S. Bigelow, and O. Benafan, "Additive manufacturing of NiTiHf high temperature shape memory alloy," *Scripta Materialia*, vol. 145, pp. 90 – 94, 2018.

[23] Thoma, P. E., Zhang, C., Boehm, J. J., and Zee, R. H., "The effect of hafnium content and cycling under an applied axial stress on the creep and martensite strain of NiTi based shape memory alloy wires," *J. Phys. IV France*, vol. 07, no. 5, pp. C5–483–C5–488, 1997.

[24] M. Belbasi, M. T. Salehi, S. A. A. A. Mousavi, and S. M. Ebrahimi, "A study on the mechanical behavior and microstructure of NiTiHf shape memory alloy under hot deformation," *Materials Science and Engineering: A*, vol. 560, pp. 96 – 102, 2013.

[25] M. M. Javadi, M. Belbasi, M. T. Salehi, and M. R. Afshar, "Effect of aging on the microstructure and shape memory effect of a hot-rolled NiTiHf alloy," *Journal of Materials Engineering and Performance*, vol. 20, pp. 618–622, Jul 2011.

[26] Olier, P., Brachet, J.C., Bechade, J.L., Foucher, C., and Guénin, G., "Investigation of transformation temperatures, microstructure and shape memory properties of NiTi, NiTiZr and NiTiHf alloys," *J. Phys. IV France*, vol. 05, no. 8, pp. C8–741–C8–746, 1995.

[27] P. Salvetr, A. Školáková, J. Kopeček, and P. Novák, "Properties of Ni-Ti-X shape memory alloys produced by arc re-melting," *Acta Metallurgica Slovaca*, vol. 23, no. 2, pp. 141–146, 2017.

[28] M. Zarinejad, Y. Liu, and T. J. White, "The crystal chemistry of martensite in NiTiHf shape memory alloys," *Intermetallics*, vol. 16, no. 7, pp. 876 – 883, 2008.

[29] C. Hayrettin, O. Karakoc, I. Karaman, J. Mabe, R. Santamarta, and J. Pons, "Two way shape memory effect in NiTiHf high temperature shape memory alloy tubes," *Acta Materialia*, vol. 163, pp. 1 – 13, 2019.

[30] F. Yang, D. Coughlin, P. Phillips, L. Yang, A. Devaraj, L. Kovarik, R. Noebe, and M. Mills, "Structure analysis of a precipitate phase in an Ni-rich high-temperature NiTiHf shape memory alloy," *Acta Materialia*, vol. 61, no. 9, pp. 3335 – 3346, 2013.

[31] P. W. Muncaster, *Practical Guide to TIG (GTA) welding.* Abington Publishing, 1991.

[32] J. Cornu, *Advanced Welding Systems - Fundamentals of Fusion Welding Technology.* Springer-Verlang Berlin Heidelberg GmbH, 1998.

[33] G. Fox, R. Hahnlen, and M. J. Dapino, "Fusion welding of nickel–titanium and 304 stainless steel tubes: Part II: tungsten inert gas welding," *Journal of Intelligent Material Systems and Structures*, vol. 24, no. 8, pp. 962–972, 2013.

[34] C. Heiple and J. Roper, "Chapter 1 - the geometry of gas tungsten arc, gas metal arc, and submerged arc weld beads," in *Welding* (D. L. Olson, R. Dixon, and A. L. Liby, eds.), vol. 8 of *Materials Processing: Theory and Practices*, pp. 1 – 34, Elsevier, 1990.

[35] R. L. Alley *et al.*, *ASM Handbook Volume 6: Welding, Brazing and Soldering.* ASM International, 1993.

[36] A. Ikai, K. Kimura, and H. Tobushi, "TIG welding and shape memory effect of TiNi shape memory alloy," *Journal of Intelligent Material Systems and Structures*, vol. 7, no. 6, pp. 646–655, 1996.

[37] K. Weman, *Welding processes handbook*. Woodhead, 2012.

[38] S. Kou, *Welding Metallurgy*. John Wiley & Sons, Inc, 2 ed., 2003.

[39] L. Jeffus, *Welding Principles and Applications*. Cengage Learning, 2015.

[40] J. Oliveira, D. Barbosa, F. B. Fernandes, and R. Miranda, "Tungsten inert gas (TIG) welding of Ni-rich NiTi plates: functional behavior," *Smart Materials and Structures*, vol. 25, no. 3, p. 03LT01, 2016.

[41] C. L. Jenney and A. O'Brien, *Welding Handbook Volume 1: Welding Science and Technology*. American Welding Society, 9 ed., 2001.

[42] S. Kou and Y. Lee, "Nucleation mechanisms and grain refining of weld metal," *The Welding Journal*, pp. 305s–313s, 12 1986.

[43] J. Oliveira, A. Cavaleiro, N. Schell, A. Stark, R. Miranda, J. Ocana, and F. B. Fernandes, "Effects of laser processing on the transformation characteristics of NiTi: A contribute to additive manufacturing," *Scripta Materialia*, vol. 152, pp. 122 – 126, 2018.

[44] ASTM F2082 / F2082M-16, "Standard test method for determination of transformation temperature of nickel-titanium shape memory alloys by bend and free recovery." ASTM International, West Conshohocken, PA, 2016. www.astm.org.

[45] H. Karaca, S. Saghaian, B. Basaran, G. Bigelow, R. Noebe, and Y. Chumlyakov, "Compressive response of nickel-rich NiTiHf high-

temperature shape memory single crystals along the [111] orientation," *Scripta Materialia*, vol. 65, no. 7, pp. 577 – 580, 2011.